Short Papers

A New Absorbing Boundary Condition Structure for Waveguide Analysis

Krishna Naishadham and Zhian Lin

***Abstract*—The existence of evanescent waves and waves near cutoff frequencies limits the accuracy of the fields computed in waveguides using the finite-difference time-domain method, and prompted several researchers to design complicated boundary conditions, including combinations of perfectly matched layers and Higdon's higher order absorbing boundary conditions (ABC's). Instead, we employ a terminating structure in which the lateral walls are made absorbing in addition to the longitudinal walls. The undesirable lateral waves at the normal boundary interface are slowed down and effectively attenuated in the lateral walls, while the propagating waves are absorbed in the longitudinal walls. Numerical calculations for pulse excitation of a rectangular waveguide, using the simple Mur's first-order ABC, demonstrate the usefulness of the method.**

***Index Terms*—Absorbing boundary conditions, evancescent waves, FDTD analysis, waveguides.**

I. INTRODUCTION

The finite-difference time-domain (FDTD) technique involves absorbing boundary conditions (ABC's) to truncate the computational domain. The recent advancements in ABC's, such as the perfectly matched layer (PML) [1], significantly decrease the residual reflection in the time domain for scattering problems, but they are not very effective in absorbing nonpropagating modes in waveguides [2]. Unlike situations in most scattering problems, evanescent waves are frequently encountered in transient analysis of waveguide structures. In time-domain analysis, the input pulse, such as a modulated Gaussian, will always have frequency components near and below cutoff, which are difficult to absorb using conventional ABC's, imposed longitudinally. While some positive results on the PML absorption of propagating waves in parallel-plate waveguides have been reported in [2], Wu and Fang [2] performed detailed analysis on longitudinal PML termination of waveguides, and demonstrated that the PML is indeed very effective in absorbing waves propagating well above cutoff frequencies, but quite ineffective in absorbing evanescent waves [6], or for that matter, *any* wave, near or below cutoff frequencies. Some improvement can be gained by combining the PML with Higdon's ABC's to provide reasonable absorption in specific directions away from the cutoff [2], which corresponds to grazing angle incidence on the longitudinal boundary.

In this paper, in order to facilitate the absorption of both evanescent and propagating modes, we employ a parallel-plate terminating structure [termed as the absorbing boundary condition structure (ABCS)], in which the lateral walls are made absorbing in addition to the longitudinal walls. The evanescent waves, as well as propagating waves near cutoff, travel laterally across the interface between free space and the longitudinal boundary. These cannot be absorbed by the traditional ABC's, imposed longitudinally. Instead, these undesirable lateral waves, a dominant source of error, are slowed down and effectively attenuated in the lateral walls, while the propagating waves are absorbed in the longitudinal walls. No lossy materials are employed for absorption. Numerical calculations for pulse excitation of a rectangular waveguide, using the simple Mur's first-order ABC, demonstrate the usefulness of the method.

For simplicity, we have chosen Mur's first-order ABC in the FDTD implementation, which also represents the worst-case scenario. However, the ABCS can reduce the error introduced by any ABC employed, with the more sophisticated ABC's perhaps resulting in higher accuracy or smaller computational domains. It is emphasized that the goal of this paper is to demonstrate the effectiveness of the new lateral ABCS in reducing the boundary reflection for evanescent waves and waves near cutoff frequencies.

II. METHODOLOGY

Uniform plane waves propagate in free space, unattenuated, and in a conducting medium, where they are slowed and attenuated in the direction of travel. One might ask whether there could be a free-space wave that is attenuated in the absence of loss. Clearly, it is well known that certain waves in metallic or dielectric waveguides can be slowed (from the speed of light) in the direction of travel, and can be matched to (slow) waves on a slow-wave structure [4]. Such wave propagation has relevance to pulse absorption near an absorbing boundary, as shown below.

Consider the regular rectangular waveguide (Fig. 1). Without loss of generality, assume that the electric field $\vec{E}$ is y-polarized. The waves propagate in the x–z plane to set up standing waves in x, so that the sidewalls can be placed at the nulls of the electric field. $\vec{E}$ will obviously have x-dependence because propagation vectors $\vec{k}_1$ and $\vec{k}_2$ (see Fig. 1) have components along x. For simplicity, let us consider the dominant mode, in which case the electric field is independent of y. With E_0 denoting the electric-field amplitude, we have

$$\vec{E} = \hat{u}_y E_0 \left(e^{-j\vec{k}_1 \cdot \vec{r}} - e^{-j\vec{k}_2 \cdot \vec{r}} \right). \tag{1}$$

The phase of the second term is chosen to cancel the fields on the sidewalls. The corresponding magnetic field is found from Fig. 1 as

$$\vec{H} = \frac{E_0}{\eta} \Big[\hat{u}_x \cos\phi \left(e^{-j\vec{k}_1 \cdot \vec{r}} - e^{-j\vec{k}_2 \cdot \vec{r}} \right) + \hat{u}_z \sin\phi \left(e^{-j\vec{k}_1 \cdot \vec{r}} + e^{-j\vec{k}_2 \cdot \vec{r}} \right) \Big] \tag{2}$$

where η is the free-space impedance. Since $\vec{k}_1 = (-k \sin\phi, 0, k \cos\phi)$ and $\vec{k}_2 = (k \sin\phi, 0, k \cos\phi)$, where $k = \omega\sqrt{\mu_0 \epsilon_0}$ is the free-space wavenumber, these fields simplify to

$$E_y = 2E_0 j \sin(kx \sin\phi) e^{-jkz \cos\phi} \tag{3}$$

$$\eta H_x = 2E_0 j \cos\phi \sin(kx \sin\phi) e^{-jkz \cos\phi} \tag{4}$$

$$\eta H_z = 2E_0 \sin\phi \cos(kx \sin\phi) e^{-jkz \cos\phi}. \tag{5}$$

If the Poynting vector were formed with $E_y H_x^*$, the result would represent real power flow down the guide, whereas $E_y H_z^*$ represents reactive power bouncing back and forth between the sidewalls at $x = 0$ and $x = a$.

Manuscript received March 18, 1998. This work was supported in part by the Air Force Research Laboratory under Contract F33615-98-C-1347.

K. Naishadham was with the Department of Electrical Engineering, Wright State University, Dayton, OH 45435 USA. He is now with Phillips Broadband Networks Inc., Syracuse, NY 13104 USA.

Z. Lin is with the Department of Electrical Engineering, Wright State University, Dayton, OH 45435 USA.

Publisher Item Identifier S 0018-9480(00)00231-3.

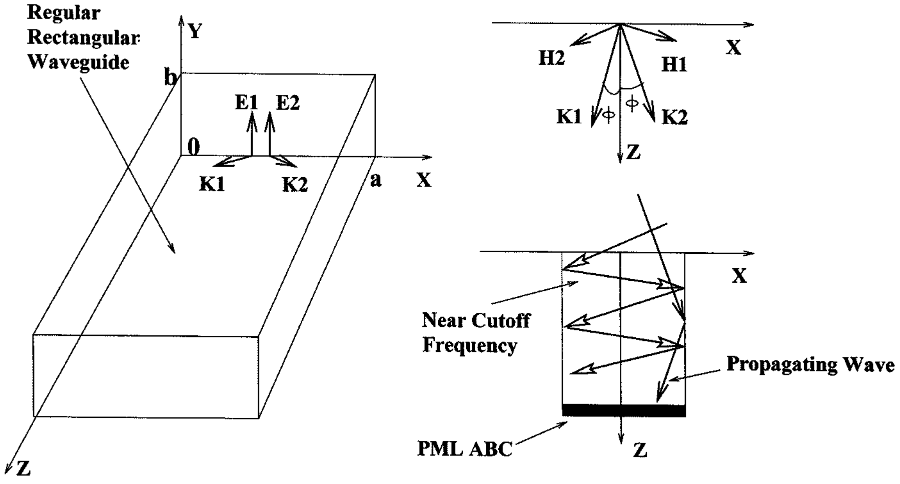

Fig. 1. Illustration of slow waves in a rectangular waveguide.

As Berenger derived [1], the $\vec{E}$-field component, after entering the PML medium along z with metallic sidewalls in the yz-plane at $x = 0$ and $x = a$, could be expressed as

$$E_y = 2E_0 j \sin(kx \sin\phi) e^{-jkz\cos\phi} e^{-(\sigma_z \cos\phi/\epsilon_0 c)z} \tag{6}$$

where

$$k \sin\phi = \frac{\pi}{a} \quad k\cos\phi = \sqrt{\omega^2 \mu_0 \epsilon_0 - \left(\frac{\pi}{a}\right)^2}. \tag{7}$$

If in the z-direction the field is propagating, then $\cos\phi$ is real, and the term $e^{-(\sigma_z \cos\phi/\epsilon_0 c)z}$ in (6) contributes to the attenuation of the field. The smaller the angle ϕ or closer to normal incidence, the larger is the attenuation in the PML [see Fig. 1, bottom right-hand side]. When the angle ϕ reaches $\pi/2$ or, equivalently, when the frequency approaches cutoff, there will be no attenuation of the wave in the PML, but the wave travels laterally in the xy-plane as a slow wave, bouncing back and forth at the sidewalls [see Fig. 1, bottom right-hand side]. Clearly, such a wave cannot be absorbed by the normal walls perpendicular to z. On the other hand, if the variation of the field in the z-direction is of evanescent nature, $\cos\phi$ will be imaginary, and the term $e^{-(\sigma_z \cos\phi/\epsilon_0 c)z}$ no longer decays the field in the z-direction. In order to design a PML for evanescent waves, Berenger [5] modified (6), but even that equation seems to work only for frequencies above a certain cutoff frequency determined by the PML conductivity. Furthermore, numerical reflections from the inner interfaces in PML's with growing conductivity corrupt the results. From the above analysis, we conclude that the (longitudinal) PML's positioned perpendicular to z in waveguides cannot absorb the waves near cutoff frequencies, obtained for incident angles around the direction $\phi = \pi/2$.

As a possible remedy, we construct an attenuated waveguide structure (Fig. 2), in which we replace the lateral perfectly conducting walls in the terminating region of the waveguide with the simple Mur's first-order ABC. The longitudinal boundary is also terminated with Mur's first-order ABC to assess the worst-case error. It is noted that the conducting walls are replaced with Mur's ABC only in a small region at the termination. Away from this termination, the sidewalls are conducting. We refer to this termination as the ABCS.

When the evanescent waves and the waves near cutoff frequencies occur or, equivalently, as the angle ϕ approaches $\pi/2$, the waves in the ABCS will propagate along x as slow waves, with wavenumber k, and not like a standing wave in the regular waveguide. These lateral waves will be absorbed effectively by the ABCS, as confirmed by the numerical results to be presented below. In comparison with the computationally intensive PML calculations [5], no boundary conductivity is involved, and the proposed ABCS leads to a simple implementation.

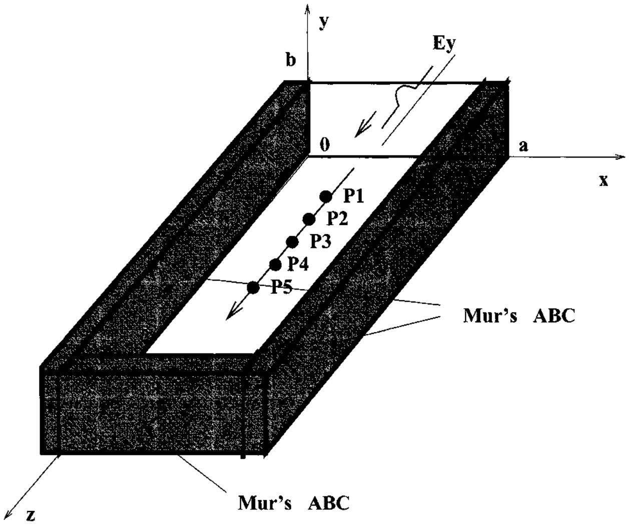

Fig. 2. New absorbing boundary structure for a rectangular waveguide.

III. SAMPLE RESULTS

A. Absorption of Evanescent Field

A Gaussian pulse, propagating along the z-direction, is impressed at the source plane ($z_0 = 40\Delta z$)

$$E_y(x, t) = \exp\left[-\frac{(t-t_0)^2}{T^2}\right] \sin\left(\frac{\pi x}{a}\right) \tag{8}$$

where $t_0 = 420\Delta t$, $T = 140\Delta t$, and $a = 2.286$ mm. These parameters are chosen such that significant energy exists below the cutoff frequency, thus exciting evanescent fields. The amplitude of the spectrum of this pulse above cutoff (for propagating modes) is very small. Hence, the propagating modes are very weakly excited. The (mostly evanescent) field E_y at the five observation planes $P1$–$P5$ (see Fig. 2), separated by ten spatial increments from $50\Delta z$ to $90\Delta z$, is calculated for the following three conditions. Initially, the four sidewalls $x = 0$, $x = a$, $y = 0$, and $y = b$ are entirely retained as perfectly conducting

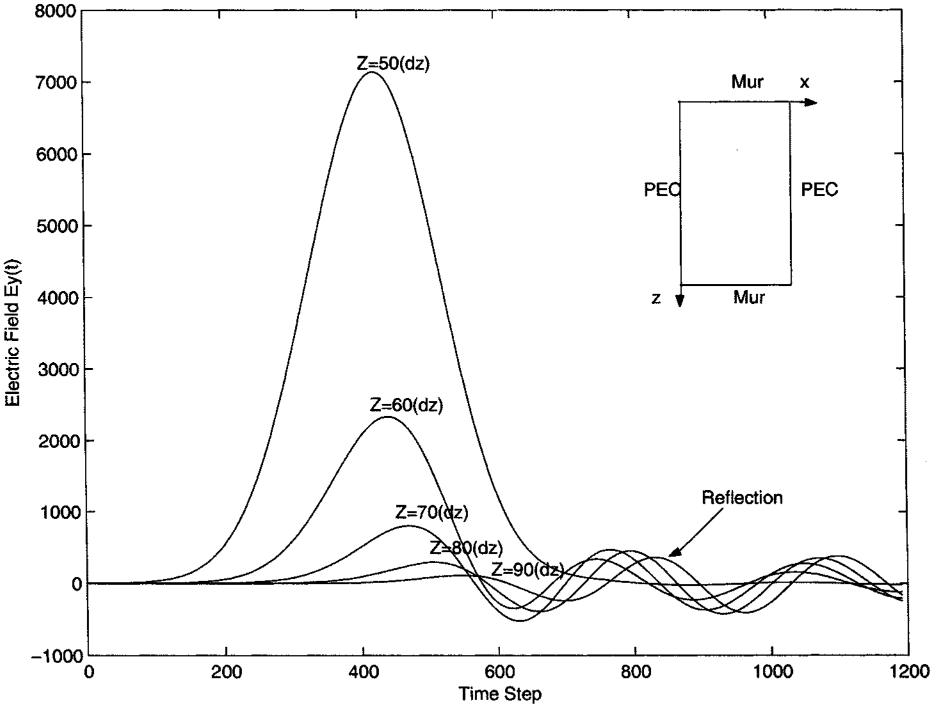

Fig. 3. Gaussian pulse propagation in a regular waveguide with all four perfectly conducting sidewalls.

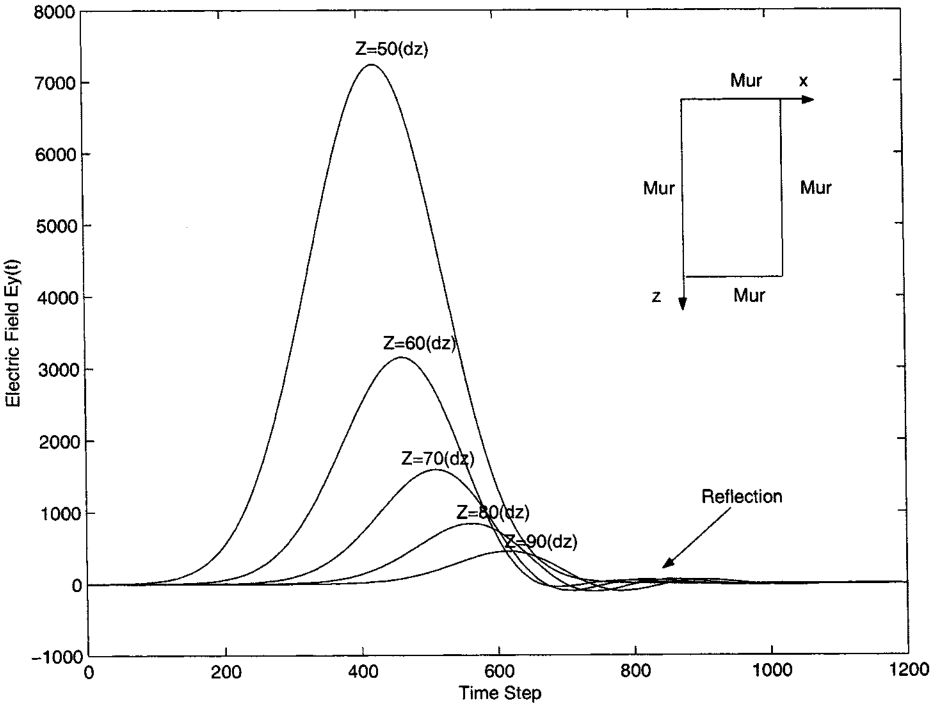

Fig. 4. Gaussian pulse propagation within the ABCS with two absorbing sidewalls at $x = 0$ and $x = a$.

while Mur's ABC is imposed on the two longitudinal walls. The time history of the field E_y, shown in Fig. 3, reveals significant pulse distortion caused by total reflection of the evanescent components at the sidewalls. Second, when we make the two sidewalls absorbing, and leave the other two (top and bottom) perfectly conducting, we obtain the response shown in Fig. 4. This configuration is the ABCS depicted in Fig. 2. We notice that the Gaussian pulse, even with significant evanescent and modal components near cutoff frequencies, will attenuate very fast without appreciable amplitude distortion or pulse dispersion. However, a small oscillation, caused by residual boundary reflection, is still observed around the trailing edge of the pulse. Nonetheless, it is clear that the reduction of reflection error in Fig. 4 is only due to the inclusion of the two absorbing lateral walls, as the longitudinal ABC is identical for Figs. 3 and 4. In the third case (Fig. 5), when we place Mur's ABC on the top wall in addition to the two sidewalls, the residual reflection practically vanishes, thus confirming the importance of reflectionless absorption of evanescent waves. Not much change is further observed when we make all four sidewalls absorbing.

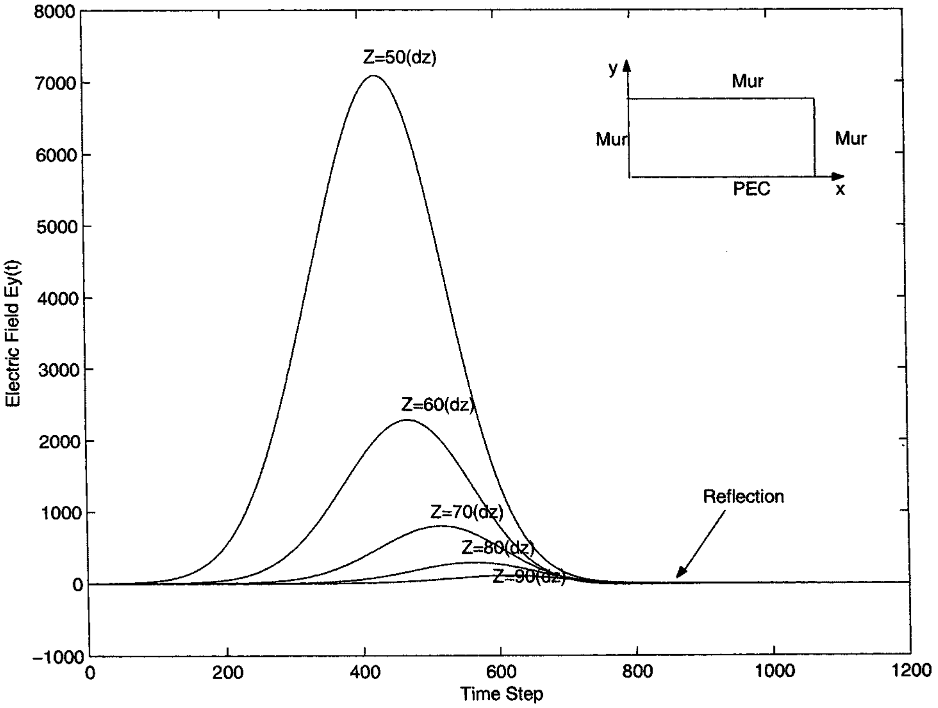

Fig. 5. Gaussian pulse propagation within the ABCS with three absorbing sidewalls at $x = 0, x = a$, and $y = b$.

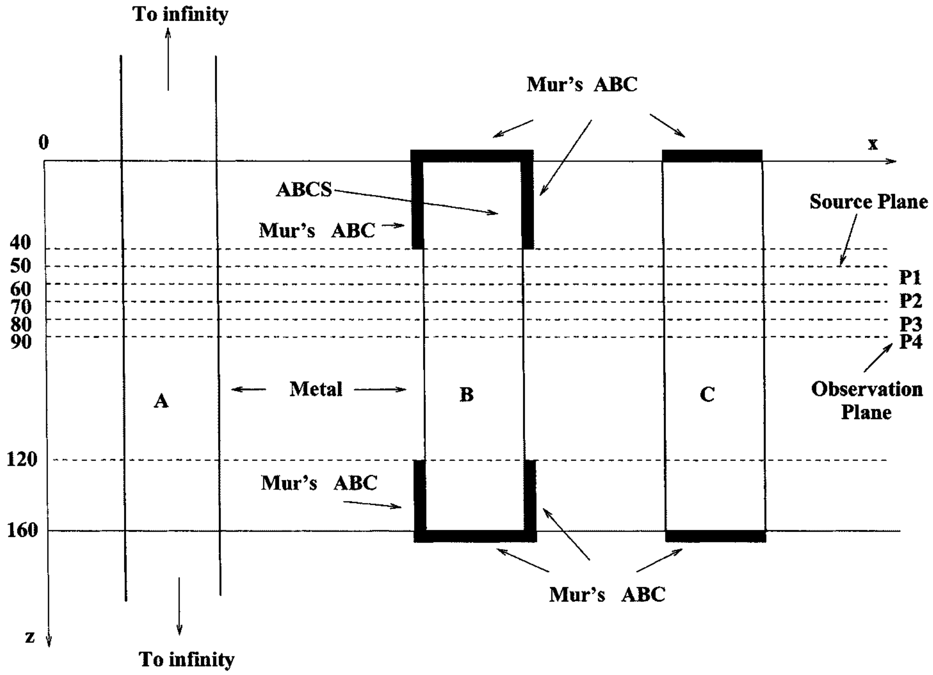

Fig. 6. Top view of three different waveguide structures.

B. Absorption of Propagating Field

We now apply a modulated Gaussian pulse with the same parameters as those in the previous section, but with a modulation frequency $f_m = f_c^{20}$, where $f_m = f_c^{20}$ is cutoff frequency of the TE_{20} mode

$$E_y(x, t) = \exp\left[-\frac{(t - t_0)^2}{T^2}\right] \sin(\omega_m t) \sin\left(\frac{\pi x}{a}\right). \tag{9}$$

This pulse has most of its energy above the cutoff frequency of the dominant TE_{10} mode. To test the effectiveness of the new ABCS for propagating modes, consider the following problem: a uniform rectangular waveguide terminated in three ways, as indicated by the top views shown in Fig. 6, where A is very long waveguide ($L = 3000\Delta z$) to generate the reference solution, B is a relatively short waveguide ($L = 160\Delta z$) with the two sidewalls $x = 0$ and $x = a$ terminated with Mur's ABC over a length $40\Delta z$ outside the metal walls, and C is a regular waveguide ($L = 160\Delta z$) with longitudinal Mur's ABC, but with perfectly conducting sidewalls over the entire length.

We apply the excitation in the plane $z_0 = 50\Delta z$ and compute transient waveforms and their corresponding frequency spectra in various

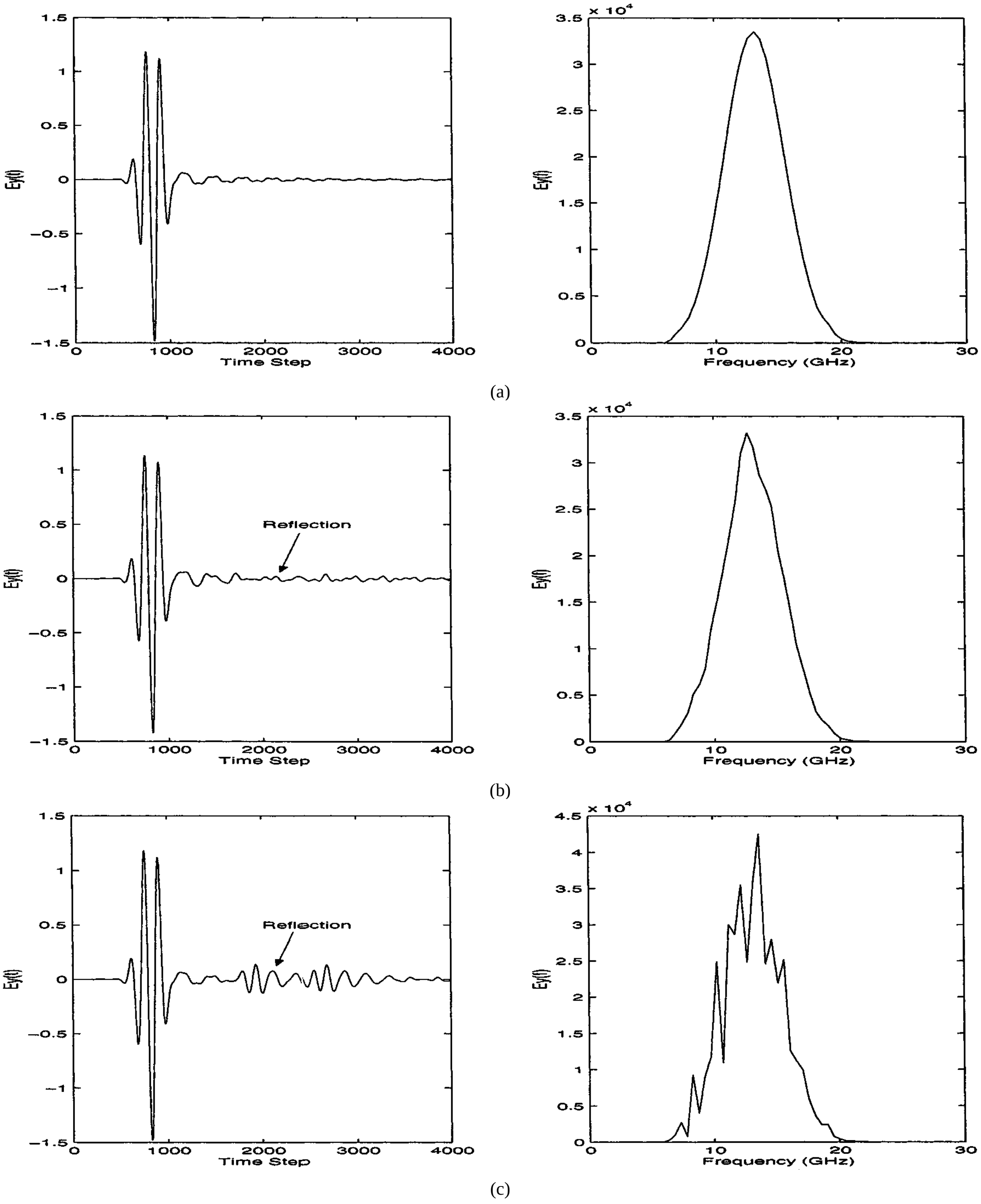

(a)

(b)

(c)

Fig. 7. Evolution of the transient waveforms and the resulting spectra for the field in plane $P4$, calculated using the three waveguide terminations shown in Fig. 6. (a) Preference solution. (b) ABCS. (c) Conventional FDTD.

transverse planes ($P1$–$P4$) shown in Fig. 6. For brevity, only the results for $z = 90\Delta z$ are displayed in Fig. 7. The conclusions are identical for the other observation planes. The reference pulse and its spectrum correspond to Fig. 7(a). The conventional FDTD with conducting sidewalls (structure C) causes significant boundary reflection (see the tail between 2000 and 3500 time steps), which results in appreciable distortion of the spectrum. On the other hand, the ABCS with two absorbing sidewalls (structure B) produces very little reflection in the tail, and the corresponding spectrum is in good agreement with most of the reference spectrum for propagating as well as evanescent fields. The worst-case reflection in the conventional method is calculated as −22 dB, whereas that in the ABCS implementation is −70 dB. Therefore, considerable improvement in computational accuracy for absorbing both propagating and evanescent waves, including those near cutoff, can be achieved with the ABCS approach.

IV. CONCLUSIONS

A novel absorbing boundary structure has been introduced for terminating waveguides in FDTD analyses. This ABCS is transparent to both propagating and evanescent waves, especially near cutoff frequencies. The ABCS is designed by replacing the conducting sidewalls in the terminal region with absorbing walls in order to match waves approaching the longitudinal boundary close to its grazing angle (grazing corresponds to cutoff frequency). Far away from the cutoff, other researchers have shown that conventional longitudinal ABC's with conducting sidewalls, such as the PML [2], perform adequately, but they reflect appreciably near and below the cutoff frequency. Our analysis shows that such reflection is indeed due to the conducting sidewalls; hence, it can be reduced by making these walls absorbing. The simulated results for Gaussian and modulated Gaussian pulse excitation, assuming a dominant mode propagation, demonstrate that considerable improvement can be obtained in the fidelity of the spectrum at all frequencies, even by using a simple Mur's first-order ABC over a small terminating region instead of the perfect electric conductor (PEC) sidewalls. The maximum reflection error over the spectrum of the pulse has been reduced to −70 dB. This can potentially lead to more accurate waveguide analyses using the FDTD method than currently available ABC's permit.

REFERENCES

[1] J. P. Berenger, "A perfectly matched layer for the absorption of electromagnetic waves," *J. Comput. Phys.*, vol. 114, pp. 185–200, Oct. 1994.

[2] Z. Wu and J. Fang, "Numerical implementation and performance of perfectly matched layer boundary condition for waveguide structures," *IEEE Trans. Microwave Theory Tech.*, vol. 43, pp. 2676–2683, Aug. 1995.

[3] C. E. Reuter, R. M. Joseph, E. T. Thiele, D. S. Katz, and A. Taflove, "Ultrawide-band absorbing boundary condition for termination of waveguiding structures in FD-TD simulations," *IEEE Microwave Guided Wave Lett.*, vol. 4, pp. 344–346, Oct. 1994.

[4] L. B. Felsen and N. Marcuvitz, *Radiation and Scattering of Waves*. Englewood Cliffs, NJ: Prentice-Hall, 1973, ch. 3.

[5] J. P. Berenger, "Numerical reflection of evanescent waves from perfectly matched layers," in *IEEE AP-S Symp. Dig.*, July 1997, pp. 1888–1891.

[6] J. Fang and Z. Wu, "Generalized perfectly matched layer for the absorption of propagating and evanescent waves in lossless and lossy media," *IEEE Trans. Microwave Theory Tech.*, vol. 44, pp. 2216–2222, Dec. 1996.

Theoretical and Experimental Study of Various Types of Compensated Dielectric Bridges for Millimeter-Wave Coplanar Applications

Eric Rius, Jean Philippe Coupez, Serge Toutain, Christian Person, and Pierre Legaud

***Abstract*—This paper describes a new approach for the integration of dielectric bridges in microwave-integrated-circuit uniplanar technology. Taking into account the electrical influence of these elements on a coplanar waveguide, a simple way to compensate these parasitic effects is presented. It consists of locally tuning the dimensions of both the bridges and associated compensation lines. Theoretical and experimental results on coplanar waveguides and T-junctions are given up to the millimeter frequency range. Finally, to validate the proposed technique, a bandpass filter including compensated dielectric bridges is implemented.**

***Index Terms*—Bandpass filters, coplanar transmission lines, millimeter-wave circuits.**

I. INTRODUCTION

Many studies have shown that the coplanar waveguide can be considered as a good alternative to microstrip lines in the millimeter frequency range [1]. However, there is one major drawback in dealing with coplanar design. The parasitic and strongly dispersive coupled slotline mode may be excited by nonsymmetrical coplanar-waveguide discontinuities, such as bends or T-junctions for example. As even and odd modes are fundamental modes for the coplanar waveguide, it is necessary to eliminate one of them, i.e., the coupled slotline mode. This is achieved by the insertion of bridges that enforce identical potential values on each side of the ground plane. Generally, bridges in microwave integrated circuits (MIC's) are implemented by thin metallic wires ($\phi \approx 25$ μm), which are bonded to the ground planes. However, such an operation induces numerous problems in reproducibility and positioning, which deteriorate the circuit performances. Moreover, the mechanical fragility of such bridges does not guarantee circuit reliability.

In this paper, we present how these problems can be overcome by using a new multilayer uniplanar approach for bridges integration. Nevertheless, dielectric bridges appear as strong discontinuities on coplanar circuits, and must be compensated. Thus, we propose a way to reduce the parasitic influence of the bridges by locally tuning the dimensions of both the bridges and associated compensation lines. We then illustrate how this technique can be successfully applied to the millimeter functions design.

II. THICK-FILM MULTILAYER UNIPLANAR TECHNOLOGY FOR DIELECTRIC BRIDGES INTEGRATION

The multilayer uniplanar technology is built by dielectric layers deposition on a substrate using a thick-film technological process. The metallic layer is then directly screen-printed, or screen-printed

---

Manuscript received May 19, 1998.

E. Rius, J. P. Coupez, and C. Person are with the Laboratoire d'Electronique et Systèmes de Télécommunications, 29285 Brest, France, and also with the Université de Bretagne Occidentale, 29285, Brest France, and the Ecole Nationale Superieure des Télécommunications de Bretagne, 29285 Bretagne, France.

S. Toutain was with the Laboratoire d'Electronique et Systèmes de Télécommunications, 29285 Brest, France. He is now with the Laboratoire des Systèmes Electronique et Informatique, 44306 Nantes, France.

P. Legaud is with the the Centre National d'Etudes des Télécommunication, 22302 Lannion, France.

Publisher Item Identifier S 0018-9480(00)00227-1.

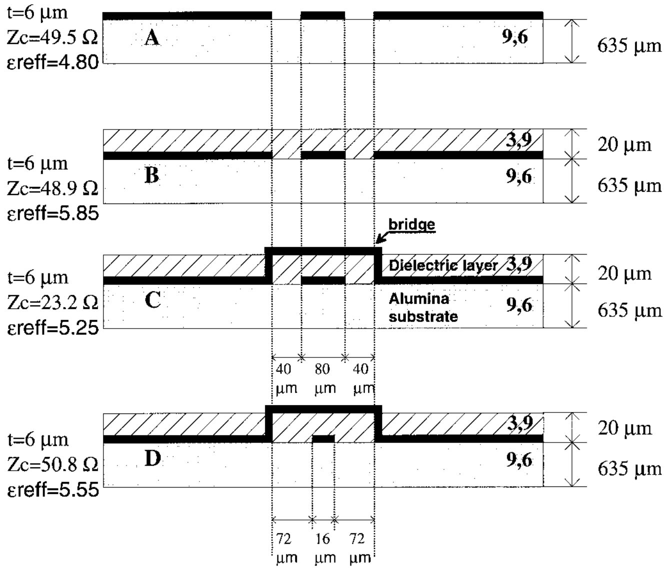

Fig. 1. Electrical parameters of the multilayer technology.

and etched, on the upper side of the dielectric layers. In our case, the dielectric material used is a photosensitive Heraeus ink (KQ 110) with a low-permittivity value equal to 3.9 and dielectric losses of 5×10^{-5} [2]. With this ink, low-loss propagation characteristics have been observed over a 1–50-GHz frequency band, with "on wafer" measurements, carried out on simple transmission lines. Finally, such a process enables us to obtain robust integrated bridges and eliminates possible problems in the positioning and reproducibility of these elements. In addition, it provides an easy control of bridge dimensions and shapes.

III. PARASITIC INFLUENCE OF THE DIELECTRIC BRIDGES

Due to the reduced height of the dielectric layers (typically between 10–20 µm for the MIC process used), an additional and significant capacitive parasitic coupling exists between the inner conductor of the coplanar waveguide and the upper short-circuited strip. Obviously, the characteristic impedance and effective permittivity of the basic coplanar waveguide are significantly modified in the bridge region. Taking into account the low dispersive characteristic of the coplanar technology, these variations can be calculated in a first approximation with a static finite-difference method [2]. In this study, bridges were modeled by an equivalent transmission line, taking into account the modified electrical parameters of this local multilayer structure. Fig. 1 shows the influence of the dielectric layer (B) and of the dielectric bridge (C) on the electrical parameters of a 50-Ω coplanar waveguide (A).

IV. COMPENSATED BRIDGES APPROACH: "LOW-PASS FILTER" CONCEPTS

To minimize the distortion due to the low characteristic impedance of the bridge discontinuity, it becomes possible to match the electrical parameters with those of the transmission line by locally reducing the inner conductor width under the bridge. Unfortunately, this method leads to obtaining very tiny strips and, consequently, increases technological constraints [see Fig. 1 (D)].

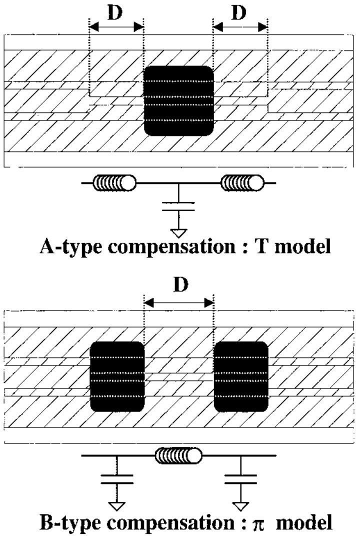

Fig. 2. "Low-pass filter" concepts.

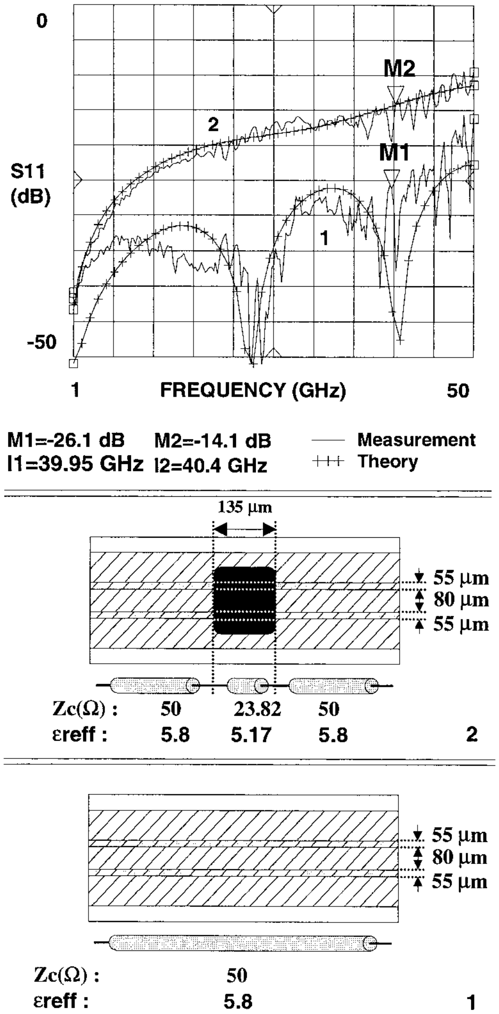

Fig. 3. Influence of a bridge on a transmission line.

Our approach is to associate high characteristic impedances on each side of the bridge to compensate its equivalent low characteristic impedance [4]. This is achieved by reducing in an appropriate way the width of both the center conductor under the bridge and the lines of length (D) on each side of it. Thus, by adjusting (D), it becomes possible to transform the bridge into an equivalent low-pass filter structure (T model) with a very high cutoff frequency. This is explained by the low L–C values model, shown in Fig. 2 (A-type

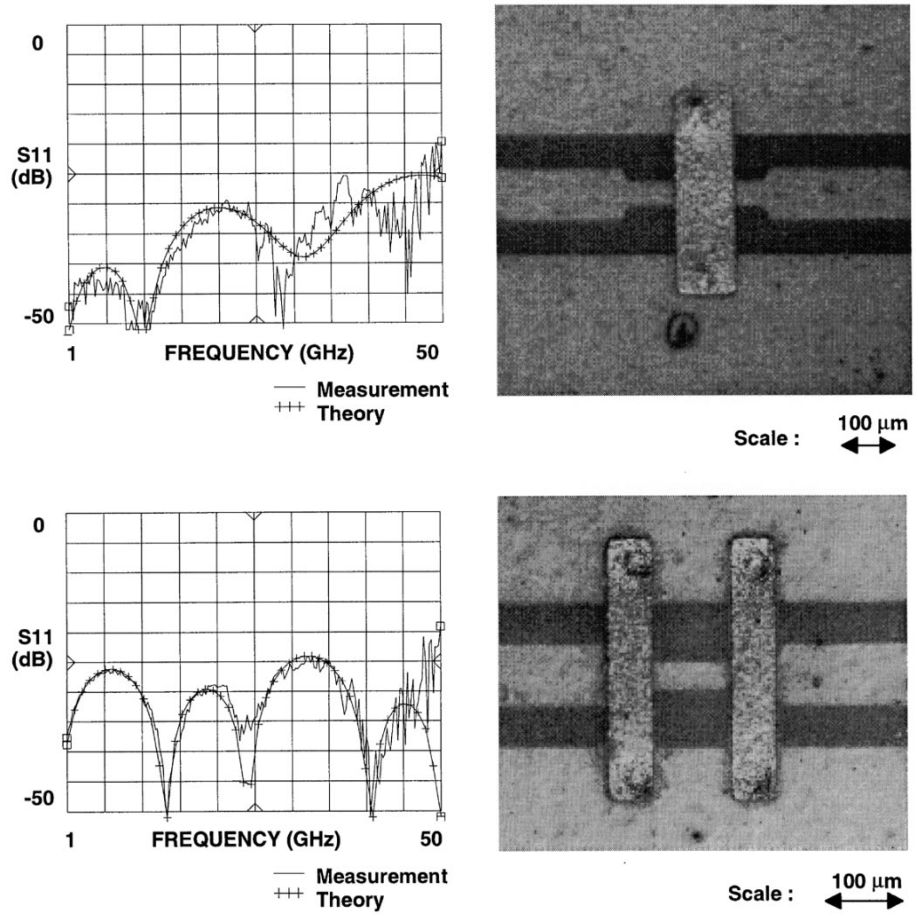

Fig. 4. A-type compensation and B-type compensation.

compensation). Based on a similar approach, the structure composed of two bridges separated by an inductive compensation element can be also realized. A low-pass filter with a π model is obtained in this case (Fig. 2: B-type compensation). The main advantage of this type of structure lies in the reduction of technological constraints: indeed, it neither requires very tiny strips nor a very precise positioning of the bridge. To validate these concepts, many different dielectric bridges configurations (with and without compensations) on 50-Ω coplanar waveguides have been built on an alumina substrate ($\varepsilon r = 9.6$, thickness $= 635$ µm). Relatively high values of the dielectric bridges lengths have been chosen especially to increase their parasitic effect on the coplanar waveguides and then to illustrate the compensation technique efficiency. "On wafer" measurements have been carried out on these structures over the 1–50 GHz frequency band. In Fig. 3, curve 1 represents return losses of a simple 50-Ω multilayer coplanar waveguide and curve 2 corresponds to the case of a similar transmission line with a 135-µm-long bridge. In this case, it should be noted that the performances strongly deteriorates. As illustrated in Fig. 4, the two types of compensation yield acceptable return losses. Moreover, the compensation technique does not produce significantly additional insertion losses.

V. COMPENSATED BRIDGES AND JUNCTIONS

Preliminary measurements were made to verify the integrated bridges efficiency in suppressing the parasitic mode on different types of discontinuities and to verify the effect of the compensation technique. For instance, Fig. 5 shows experimental results of an asymmetric short-circuited stub (theoretically, a 30-GHz resonator). The dielectric bridges modify the electrical performances of the resonator, its response is shifted to a lower frequency (20 GHz). Thus, by using a compensation technique, the resonant frequency is corrected to the required value.

VI. APPLICATION TO MILLIMETER-WAVE BANDPASS FILTERS

Finally, to validate the above compensated bridges concepts, we designed basic microwave functions such as filters that use integrated bridges. For instance, Fig. 6 deals with a classical short-circuited stubs bandpass filter [5] integrated by using a multilayer technology. In this case, bridges are thus compensated. To illustrate the flexibility of the compensation technique, two different filter prototypes were tested. A first prototype (A) uses, for example, a 60-µm-long bridge on the central resonator. The compensation of the second prototype (B) was determined in relation with the 100-µm bridge located on this central resonator. Indeed, the bridges dimension, for instance, is not critical because it is always possible to modify their lengths by adjusting the associated compensation. For the two filters, the frequency responses are identical. We only present in Fig. 6 the measurements relative to the second prototype (B). Experimental results are in agreement in both magnitude and phase with the desired response. Some discrepancies appear at high frequencies (between 40–50 GHz), but they are due to calibration errors during the measurements.

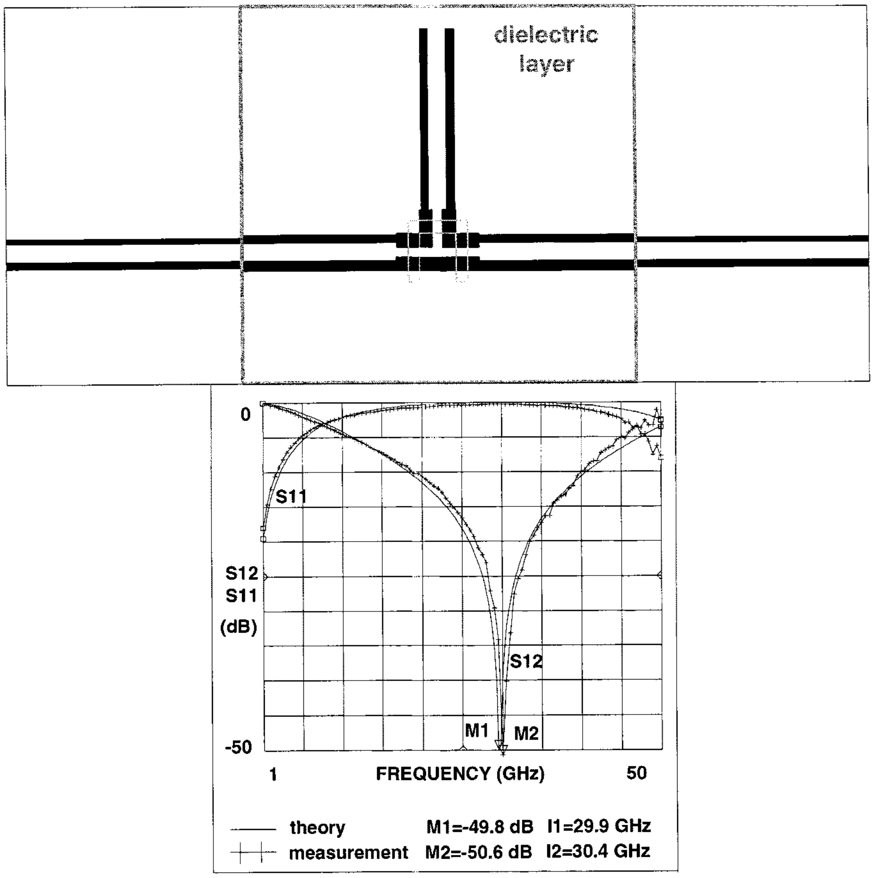

Fig. 5. Compensation technique on discontinuities.

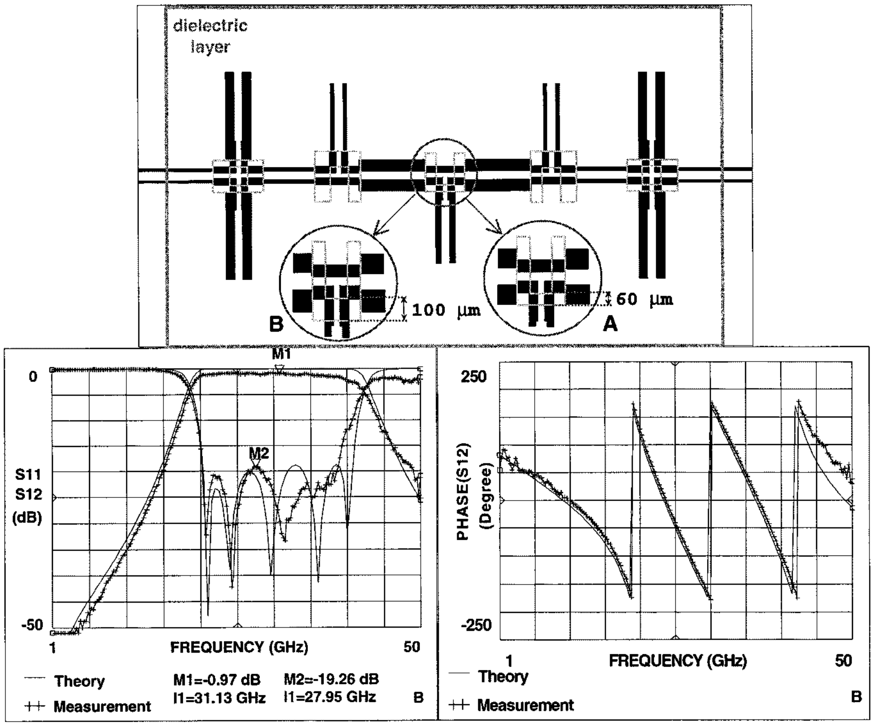

Fig. 6. Experimental and theoretical results on a compensated multilayer coplanar bandpass filter.

VII. Conclusion

Compared to the classical uniplanar technology, one main advantage of the multilayer uniplanar technology is to provide robust and reproducible integrated bridges. Indeed, with this new technology it becomes possible to control both the shape and dimensions of bridges. Thus, it is easier to model their parasitic effects on the fundamental propagation mode. Furthermore, a broad-band compensation technique has been developed and successfully applied to optimize the bridges integration on a coplanar structure. The fair agreement between theoretical and experimental results on millimeter-wave filter structures, for example, shows that a static analysis coupled with a transmission-line approach is sufficient up to 50 GHz. Consequently, this method can be very easily included in commercial computer-aided design (CAD) softwares.

Acknowledgment

The authors thank the CNET, Lannion, France, for providing "on wafer" measurements and Prof. M. Ney for his helpful suggestions.

References

[1] M. Houdart, "Coplanar lines: Application to broadband microwave integrated circuits," in *7th EuMC Dig.*, Prague, Czech Republic, 1976, pp. 49–53.

[2] P. Barnwell and G. Shorthouse, "High performance material technologies for advanced circuit assemblies and MCMs," *Microelectron. Int. J. ISHM Europe*, no. 38, pp. 28–31, Sept. 1995.

[3] M. Naghed and I. Wolff, "Equivalent capacitances of coplanar waveguide discontinuities and interdigited capacitors using a three-dimensional finite difference method," *IEEE Trans. Microwave Theory Tech.*, vol. 38, pp. 1808–1815, Dec. 1990.

[4] L. Stephan, J. P. Coupez, E. Rius, C. Person, and S. Toutain, "Integration of various types of compensated dielectric bridges for mm coplanar applications," in *IEEE MTT-S Int. Microwave Symp. Dig.*, San Francisco, CA, 1996, pp. 83–86.

[5] G. L. Matthaei, L. Young, and E. M. T. Jones, *Microwave Filters, Impedance-Matching Networks and Coupling Structures*. Norwood, MA: Artech House, 1980, sec. 10.03, pp. 595–605.

Experimental Verification of Pattern Selection for Noise Characterization

S. Van den Bosch and L. Martens

***Abstract*—A comparison is made between different pattern-selection procedures for noise characterization based on measurements of cold-FET's in a common-source configuration. The measurements were performed using an automated noise setup with one electro-mechanical tuner. The results confirm that a recently developed two-step pattern allows more accurate noise-parameter determination compared to existing practice. The significance of this paper lies in the confirmation of the simulation results presented earlier.**

***Index Terms*—MESFET's, noise, noise characterization.**

I. Introduction

During the last decade, the tendency towards smaller device dimensions and the need for more accurate device noise modeling has given increasing importance to measurement of the device's noise behavior. For measurements, the multiimpedance technique originally proposed by Lane [1] is generally accepted. State-of-the-art noise measurement setups use electronic or electro-mechanical impedance tuning to generate impedance patterns for the determination of the noise parameters. Most researchers acknowledge the influence of the source reflection-coefficient pattern on the parameter-extraction stability and the simulation accuracy [2]–[4]. Recently, an improved method was reported to select the impedance points for noise-parameter determination [5]. This method was developed based on simulation only. We now provide measurement verification to confirm the results obtained by simulation.

II. Measurements

Measurements were performed on GaAs MESFET's with a 0.7-µm gate length in common-source cold-FET configuration. For this configuration, noise parameters can be obtained directly from measured S-parameters, similarly to what is proposed in [6]. This allows an absolute verification of the noise measurement accuracy to within the S-parameter uncertainty. Common-source FET's have the disadvantage of producing much higher minimum noise figures than common-gate FET's. They are, however, more readily available.

Noise parameters were determined using a Focus Microwaves automatic noise parameter setup (Fig. 1) with one electro-mechanical tuner. At first, three impedance patterns were considered: a two-step pattern, a cross pattern with 0° angle, and a cross pattern with 45° angle. All three patterns consisted of nine points, which are shown in Fig. 2. The two-step pattern is different for each frequency since four of its points are selected using on a preliminary extraction based on the first five points. In addition, the sum of both cross patterns (17 points) was also considered. The software that drives the setup also provides an auto-noise feature that automatically selects the impedance points. Results using this feature were also included, thus providing a comparison with currently commercially available solutions.

Noise parameters were determined from 4–10 GHz for three different device geometry types: a 4 × 100 µm device and two devices

---

Manuscript received September 22, 1998. The work of S. Van den Bosch was supported by the IWT.

The authors are with the Department of Information Technology, University of Gent, B-9000 Gent, Belgium.

Publisher Item Identifier S 0018-9480(00)00228-3.

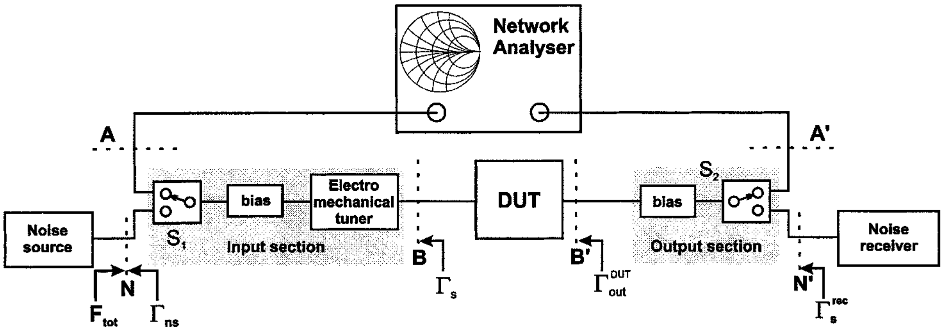

Fig. 1. Schematic of the noise setup with one electro-mechanical tuner from Focus Microwaves. The network analyzer we used is the HP 8510 and the noise receiver is a Rhode & Schwarz FSEM-30 with Miteq LNA.

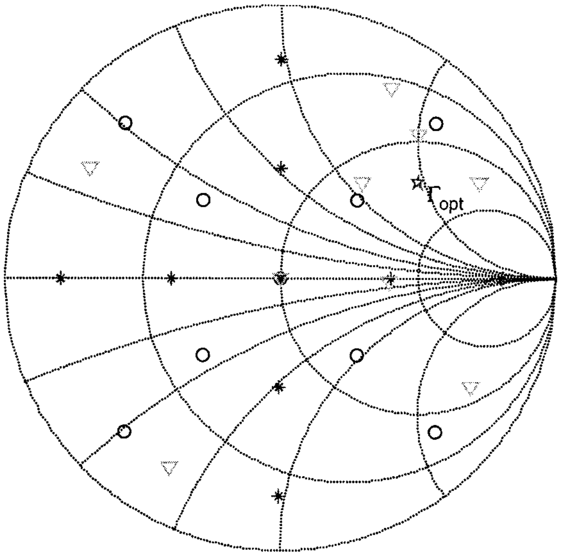

Fig. 2. Cross pattern with 0°(*) and 45°(o) angle two-step pattern (∇) and optimum source reflection coefficient $\Gamma_{\rm opt}(\star)$.

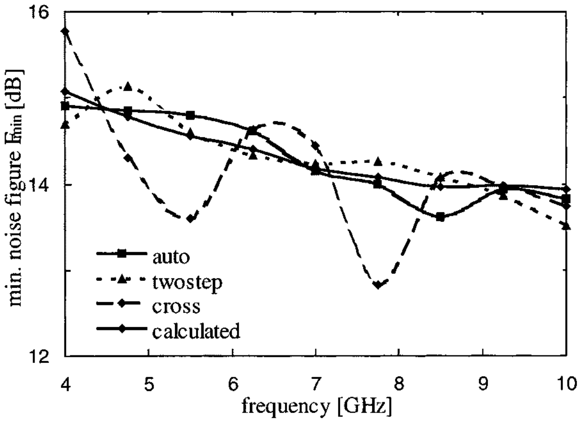

Fig. 3. Minimum noise figure for a 2 × 100 μm floating gate GaAs MESFET with a 0.7-μm gate length. A comparison is made between extracted values for three different impedance patterns and results calculated from measured S-parameters.

TABLE I
AVERAGE RELATIVE ERRORS ON THE NOISE PARAMETERS

αε	auto	two-step	cross0	cross45	cross
F_{min}	1.0%	1.3%	3.1%	4.6%	3.2%
R_n	2.2%	2.4%	2.1%	2.0%	1.8%
$\lvert\Gamma_{opt}\rvert$	2.8%	1.5%	4.5%	7.5%	4.0%
$<(\Gamma_{opt})$	1.9%	0.9%	2.2%	3.5%	2.4%

with a floating-gate in addition to their 4 μm × 100 μm and 2 × 100 μm conventional gates. The noise-parameter extraction was done using the technique proposed by Lane [1].

III. RESULTS

As an example, the extracted minimum noise figure for the 2 × 100 μm floating gate device is shown in Fig. 3.

Fig. 3 seems to indicate that for this particular device and parameter, the auto-noise and two-step pattern seem to give the best results. For each parameter, $F_{\min}$, R_n, $\mathrm{mag}(\Gamma_{\rm opt})$ and $\mathrm{phase}(\Gamma_{\rm opt})$, a percentage error $\varepsilon_P(P = F_{\min}, R_n, |\Gamma_{\rm opt}|$ or $<(\Gamma_{\rm opt}))$ is defined as the relative error with respect to the value calculated from the S-parameters. The relative errors are then evaluated as a function of frequency and the maximum ($\mu\varepsilon$) and average ($\alpha\varepsilon$) error is calculated. For the 2 × 100 μm floating gate device, the average and maximum percentage errors for all four parameters and for each of the impedance patterns are given in Tables I and II. From Tables I and II, three conclusions can be drawn. First, the minimum noise figure $F_{\min}$ is determined almost equally well by the auto noise feature and the two-step pattern. Second, R_n accuracy is worst for the two-step pattern. No conclusion can be drawn regarding the best accuracy for R_n since this differs for different devices. Finally, the two-step pattern is by far the most accurate one for determining $\Gamma_{\rm opt}$ in both magnitude and phase. These results confirm the conclusions made in [5] regarding the area of the Smith chart where each of the impedance patterns offers the greatest accuracy. The two-step pattern is the most accurate one for $F_{\min}$ and $\Gamma_{\rm opt}$ and will provide the most accurate simulation in a more or less large area around $\Gamma_{\rm opt}$. The cross patterns are more accurate on R_n, which means that for a certain distance from $\Gamma_{\rm opt}$, they will always give the most accurate simulations.

The average percentage errors on all parameters are then combined by a root sum of squares to a total average percentage error $\tau\alpha\varepsilon$, which is used in Table III to compare the three different device geometry types.

From Table III, we conclude that the patterns behave in the same way for different devices. From this, we derive confidence in the universal applicability of the conclusion drawn earlier.

TABLE II
MAXIMUM RELATIVE ERRORS ON THE NOISE PARAMETERS

$\mu\varepsilon$	auto	two-step	cross0	cross45	cross
F_{min}	2.5%	2.9%	7.7%	11.4%	8.8%
R_n	5.6%	9.4%	8.0%	6.9%	7.4%
$\lvert\Gamma_{opt}\rvert$	7.3%	3.7%	11.4%	31.7%	10.7%
$<(\Gamma_{opt})$	5.9%	1.9%	6.0%	9.1%	6.8%

TABLE III
TOTAL AVERAGE RELATIVE ERROR FOR 3 DEVICES

	auto	two-step	cross0	cross45	cross
4x100	8.6%	5.7%	9.4%	6.8%	6.5%
2x100f	2.1%	1.6%	3.1%	4.8%	3.0%
4x100f	8.8%	3.9%	5.2%	6.6%	5.3%

IV. CONCLUSION

We performed noise-parameter measurements on GaAs MESFET's in common-source cold-FET configuration with different input impedance patterns. For each pattern, noise-parameter extraction was performed using Lane's method, and the extracted parameters were compared to calculations based on measured S-parameters. Conclusions drawn from simulations only in our earlier work were confirmed: the two-step pattern offers the best overall extraction of individual noise parameters and the most accurate simulation of noise figures in the neighborhood of $\Gamma_{\rm opt}$. It also outperforms a commercially available auto-noise feature for impedance pattern selection.

REFERENCES

[1] R. Q. Lane, "Determination of device noise parameters," *Proc. IEEE*, vol. 57, pp. 1461–1462, Aug. 1969.

[2] M. Sannino, "On the determination of device noise and gain parameters," *Proc. IEEE*, vol. 67, pp. 1364–1366, Sept. 1979.

[3] A. C. Davidson, B. W. Leake, and E. Strid, "Accuracy improvements in microwave noise parameter measurements," *IEEE Trans. Microwave Theory Tech.*, vol. 37, pp. 1973–1978, Dec. 1989.

[4] J. M. O'Callaghan and J. P. Mondal, "A vector approach for noise parameter fitting and selection of source admittances," *IEEE Trans. Microwave Theory Tech.*, vol. 39, pp. 1376–1381, Aug. 1991.

[5] S. Van den Bosch and L. Martens, "Improved impedance pattern generation for automatic noise parameter determination," *IEEE Trans. Microwave Theory Tech.*, vol. 46, pp. 1673–1678, Nov. 1998.

[6] L. Escotte, R. Plana, J. Rayssac, O. Llopis, and J. Graffeuil, "Using cold FET to check accuracy of microwave noise parameter test set," *Electron. Lett.*, vol. 27, pp. 833–835, May 1991.

Mode Conversion at GCPW-to-Microstrip-Line Transitions

Jean-Pierre Raskin, Gildas Gauthier, Linda P. Katehi, and
Gabriel M. Rebeiz

***Abstract*—Mode conversion at the transition between grounded coplanar waveguide (GCPW) and microstrip line is demonstrated. Experimental results show the effect of overmoding in a conductor-backed coplanar waveguide on the transition behavior. A simple micromachining solution is used to cancel the parasitic modes triggered by the transition in the GCPW feed line. This results in an insertion loss of 0.3 dB and a return loss better than –18 dB from 75 to 110 GHz. The transition can prove very useful for millimeter-wave packaging and interconnects.**

***Index Terms*—Integrated-circuit packaging, millimeter wave, passive circuits, transmission-line discontinuities.**

I. INTRODUCTION

At millimeter- and submillimeter-wave frequencies, coplanar waveguides (CPW's) provide many solutions to the design of low-loss, uniplanar, low-cost, and compact integrated circuits. However, many applications such as on-wafer measurements of microstrip circuits or vertically integrated circuits require the flexibility to use combination of planar technologies (microstrip, coplanar waveguide, etc.). Low-loss, wide-band, and small transitions are, therefore, necessary to ensure the compatibility of CPW and microstrip technologies. CPW-to-microstrip transitions based on electromagnetic coupling are described in [1]–[2]. These transitions use a finite ground plane limited underneath the transition and the microstrip line, however, in practice, additional conducting planes are often present above or below the substrate in order to electromagnetically separate the circuit from its environment. The standard CPW plus the lower conducting plane is commonly called conductor-backed or grounded coplanar waveguide (GCPW). In this paper, the moding problem that this conductor introduces is demonstrated and resolved using a micromachined cavity underneath the grounded CPW feed line.

II. CPW AND GCPW-TO-MICROSTRIP TRANSITIONS

A. CPW-to-Microstrip Transition

Fig. 1(a) and (b) show the two main designs of CPW-to-microstrip transitions based on electromagnetic coupling presented in the literature [2], [2]. These transitions are designed following the procedure described by Pavlidis *et al.* [4], which considers the coupling region (transition) as a six-port network with a ground plane, or as three coupled-microstrip-lines [Fig. 1(a) and (b)]. In this configuration, ports 2 and 5 are the input and output ports, respectively. The transition is $\lambda_g/4$ long at the center frequency (f_o) of operation, where λ_g is the guided wavelength of the three-conductor line. Ports 4 and 6 are terminated by an open circuit, which results in ports 1 and 3 being short circuited at f_o. The system is characterized by three mode impedances (Z_{oe}, Z_{oe}, and Z_{ee}), which are calculated from the two-dimensional (2-D) quasi-static capacitances [4]. The dimensions of each coupled line are calculated to optimize the insertion and return losses of the transition, referenced

---

Manuscript received November 6, 1998. This work was supported by Hughes/Defense Advanced Research Projects Agency under Contract FR-573420-SR8.

The authors are with the Electrical Engineering and Computer Science Department, The University of Michigan at Ann Arbor, Ann Arbor, MI 48109-2122 USA.

Publisher Item Identifier S 0018-9480(00)00229-5.

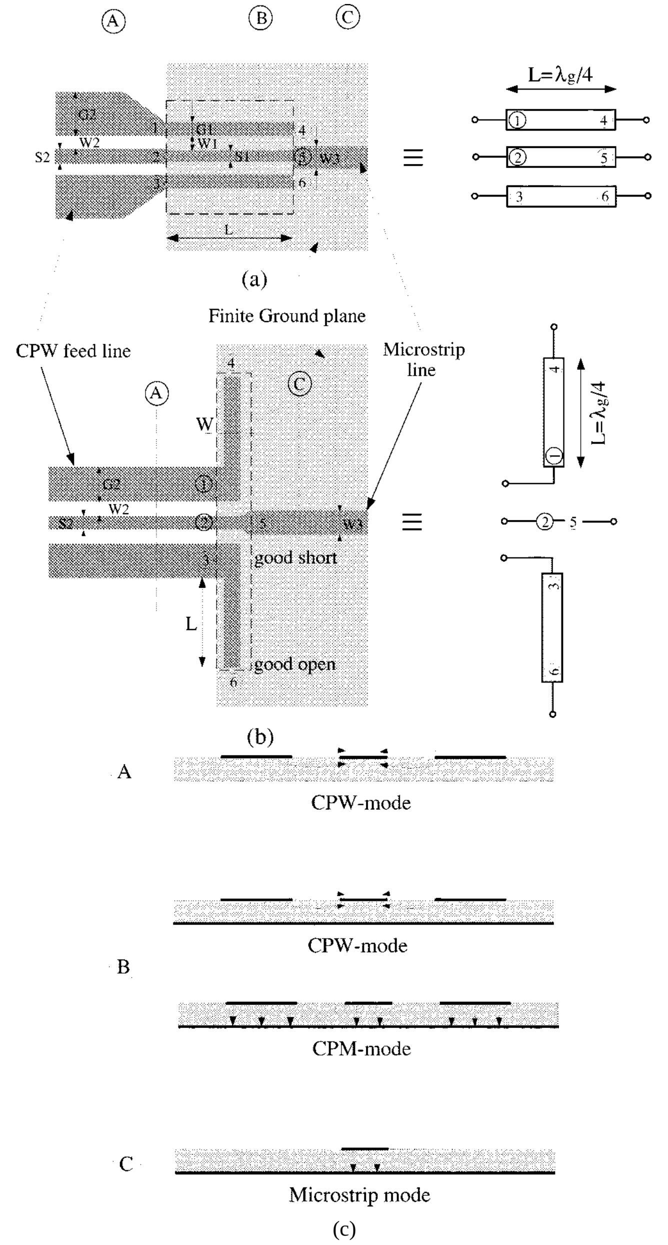

Fig. 1. CPW-to-microstrip transition layouts. (a) Gauthier's design [2]. (b) Strauss's design [2]. (c) Electric-field configuration in the different section lines.

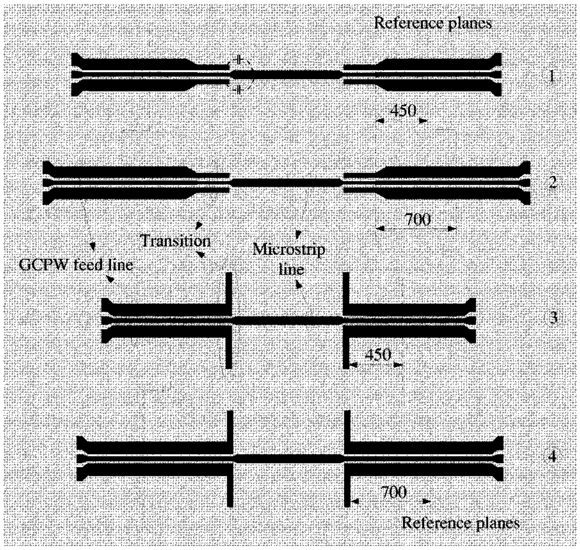

Fig. 2. Layout of the GCPW-to-microstrip-line transitions: straight open stubs (designs 1 and 2) and 90° open stubs (designs 3 and 4). All dimensions are in micrometers.

TABLE I
CHARACTERISTIC IMPEDANCE VALUES FOR THE PROPAGATION MODES IN THE NONMICROMACHINED AND MICROMACHINED GCPW FEED LINE

	standard GCPW	micromachined GCPW
Z_{CPW}	49 Ω	51 Ω
Z_{CPMc}	63 Ω	188 Ω
Z_{CPMg}	167 Ω	452 Ω

to 50-Ω input/output CPW/microstrip lines. The electric-field configurations in the cross sections labeled A, B, and C in Fig. 1(a) and (b) are represented in Fig. 1(c). There is a pure CPW mode in the CPW feed line, a pure microstrip mode along the microstrip line, and a combination of these two modes in the transition region. The transition presented in Fig. 1(a) was designed and tested in W-band frequencies by Gauthier *et al.* [2]. The transition was built on a 100-µm-thick high-resistivity silicon substrate and used a finite ground plane limited underneath the transition and microstrip line (Fig. 1). The CPW input line dimensions are $S2 = 40$ μm, $W2 = 24$ μm, and $G2 = 106$ μm corresponding to a characteristic impedance of 50 Ω. The 50-Ω microstrip line is $W3 = 74$ μm wide. The coupling region is chosen to be $L = 280$ μm long ($\lambda_g/4$ at 94 GHz) with dimensions $S1 = 28$ μm, $W1 = 30$ μm, and $G1 = 46$ μm wide (Fig. 1), corresponding to fundamental mode impedances of $Z_{oo} = 13$ Ω, $Z_{oe} = 130$ Ω, and $Z_{ee} = 50$ Ω. The evaporated metal is 8000 Å of gold, corresponding to around three skin depths at 94 GHz. The transition results in 0.3-dB insertion loss at 94 GHz with a bandwidth of 20% and a return loss better than −17 dB from 85 to 100 GHz (see [2] for more details). Strauss *et al.* [2] obtained a more wide-band CPW-to-microstrip transition at K-band frequencies using the design shown in Fig. 1(b).

The two transitions presented in Fig. 1 use a finite ground plane limited below the transition and the microstrip line. However, in practice, additional conducting planes are often present above or below the substrate in order to electromagnetically separate the circuit from its environment. In Section II-B, the influence of a ground plane below the CPW feed line is studied and solved.

B. GCPW-to-Microstrip Transition

The transitions described above are fabricated on 100-µm-thick high-resistivity silicon substrate and mounted on a metallized silicon substrate to provide the ground plane that extends everywhere (Fig. 2). Vector network analysis (VNA) measurements of back-to-back transitions separated by a 1-mm-long 50-Ω microstrip line are made using thru-reflection line (TRL) calibration techniques. The measured results of the GCPW-to-microstrip transitions for two different GCPW feed line lengths are presented in Fig. 3. Straight and 90° open stubs are used for designs 1–2 and 3–4, respectively. The transition dimensions of designs 1 and 2 are given in Section II-A. The width ($W = 50$ μm) and length ($L = 280$ μm) of the 90° open stubs have been numerically

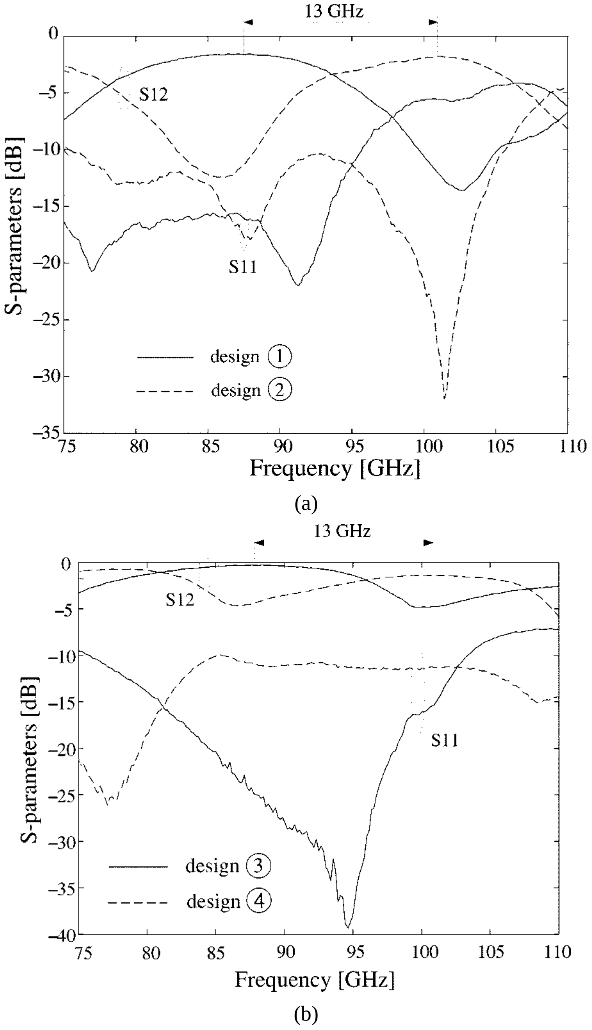

(a)

(b)

Fig. 3. Measured W-band S-parameters of back-to-back GCPW-to-microstrip transitions. (a) Designs 1 and 2. (b) Designs 3 and 4.

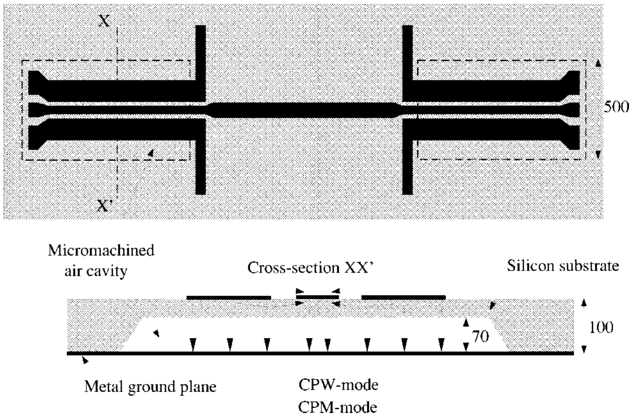

Fig. 4. Layout of the micromachined GCPW-to-microstrip line transitions and electric-field configuration in the GCPW feed line. All dimensions are in micrometers.

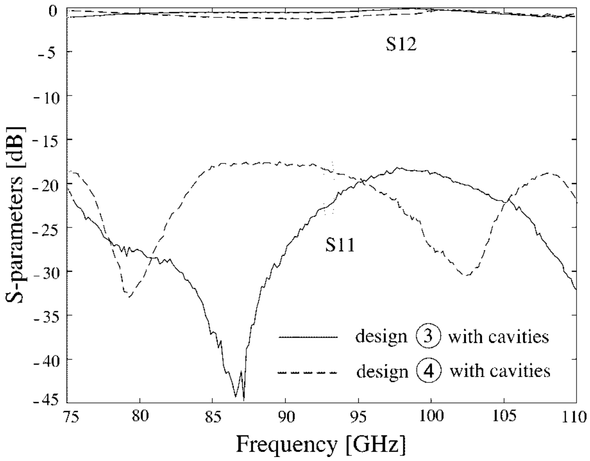

Fig. 5. Measured S-parameters of back-to-back micromachined GCPW-to-microstrip transitions versus the GCPW feed line length.

optimized using IE3D[1] for the 75–110-GHz frequency band. It clearly appears that the center frequency and bandwidth of the transition shift versus the GCPW feed-line length. This dependence is due to the propagation of a coplanar microstrip mode (CPM) along the GCPW feed line. The physical structure of the GCPW input line is similar to the transition (region) and, therefore, CPW and CPM modes can propagate in the GCPW and transition regions. In this case, the coupling region length is not only defined by the transition length L, but also by the length of the GCPW feed line.

The CPM-modes power injected in the GCPW line depends on the value of the parasitic microstrip current at points 1 and 3 (Fig. 1). The microstrip current components will be zero at these points if a pure open circuit exist at the end of the transition stubs (points 4 and 6 in Fig. 1). In the case of the designs 1 and 2, there is a substantial proximity capacitance between the straight open stubs and microstrip line. Better open circuits at points 4 and 6 are achieved using the CPW-to-microstrip line of Fig. 1(b) (designs 3 and 4). The measurements of Fig. 3 clearly show that the transition of Fig. 1(b) (vertical stubs) is better than that of Fig. 1(a) (horizontal stubs). However, this is still not suitable for monolithic microwave integrated circuits (MMIC's). Generally, via holes are used to establish a RF short between the bottom ground plane and top ground plane of the GCPW line, and this suppresses the propagation of the parasitic CPM modes in the GCPW feed line. We present here a different approach built without the use of any via holes and suitable for millimeter-wave applications.

III. SUPPRESSION OF CPM-MODES IN FEED GCPW LINE

The electromagnetic power coupled to the CPM mode will be negligible if the characteristic impedance of this mode in the GCPW feed line is much higher or lower than 50 Ω. To reach this condition we have to modify the electrical characteristics of the silicon substrate (underneath the GCPW feed line) for the CPM mode without changing the 50-Ω characteristic impedance for the CPW mode. These conditions are satisfied by etching an air cavity underneath the GCPW feed line. Cavities with dimensions of 70-μm deep and 500-μm wide have been etched using TMAH or KOH wet etching techniques in the 100-μm silicon wafer [5]. The CPW (noted Z_{CPW}) and CPM (noted $Z_{\mathrm{CPM}c}$ for the center conductor and $Z_{\mathrm{CPM}g}$ for the coplanar ground planes) mode impedances are calculated from the 2-D quasi-static capacitances. The values of the characteristic impedances for the different propagation modes in the GCPW feed line are summarized in Table I for a 100-μm full silicon wafer and for the micromachined GCPW line (Fig. 4). The etched cavities below GCPW feed lines increase the characteristic impedances of CPM modes by a factor three without affecting the propagation of

---

[1] IE3D Version 4, Zeland Software Inc., Fremont, CA.

the useful CPW mode. Fig. 5 presents the measured S-parameters of back-to-back micromachined GCPW-to-microstrip transitions using two 90° open stubs (Fig. 4) for two different GCPW feed-line lengths. The results demonstrate excellent W-band transitions, and show the efficiency of the micromachined cavities to suppress the parasitic CPM modes in the GCPW input lines. The total measured loss for the two measured back-to-back transitions is around −1 dB with a return loss for back-to-back transitions below −18 dB over 75–110 GHz. The measured loss for the GCPW line is 0.3 dB/mm at 94 GHz and, therefore, the extracted insertion loss per transition is approximately 0.3 dB from 75 to 110 GHz.

IV. CONCLUSION

Conversion modes at grounded CPW-to-microstrip transitions have been demonstrated. The CPM modes triggered at the transition in the GCPW feed lines are responsible of transition frequency shifts versus the GCPW feed-line length. The use of a simple micromachining solution is presented in this paper. Very wide-band and low-loss GCPW-to-microstrip transitions have been designed, fabricated, and tested in W-band frequencies. These transitions can prove very useful for millimeter-wave packaging and interconnects without any via-hole processing.

REFERENCES

[1] M. Houdart and C. Aury, “Various excitation of coplanar waveguide,” in *IEEE-MTT -S Int. Microwave Symp. Dig.*, 1979, pp. 116–118.
[2] G. Strauss, P. Ehret, and W. Menzel, “On-wafer measurement of microstrip-based MIMIC’s without via holes,” in *IEEE-MTT-S Int. Microwave Symp. Dig.*, 1996, pp. 1399–1402.
[3] G. P. Gauthier, L. P. Katehi, and G. M. Rebeiz, “W-band finite ground coplanar waveguide (FGCPW) to microstrip line transition,” in *IEEE-MTT-S Int. Microwave Symp. Dig.*, 1998, pp. 107–109.
[4] D. Pavlidis and H. L. Hartnagel, “The design and performance of three-line microstrip couplers,” *IEEE Trans. Microwave Theory Tech.*, vol. MTT-24, pp. 631–640, Oct. 1976.
[5] K. E. Peterson, “Silicon as a mechanical material,” *Proc. IEEE*, vol. 70, pp. 420–457, May 1982.

W-Band Single-Layer Vertical Transitions

Jean-Pierre Raskin, Gildas Gauthier, Linda P. Katehi, and
Gabriel M. Rebeiz

***Abstract*—Vertical single-layer transitions operating at W-band frequencies have been developed. The designs are uniplanar, use electromagnetic coupling, and do not require via holes or air bridges. The first transition uses coplanar-waveguide-mode coupling and results in an insertion loss of better than 0.6 dB over the whole band, with a loss of 0.25 dB from 85 to 110 GHz. The return loss is better than −10 dB from 75 to 110 GHz. The second transition uses microstrip-mode coupling and results in a 0.2-dB insertion loss over the whole W-band. These transitions can prove very useful for millimeter-wave packaging and vertical interconnects.**

***Index Terms*—Integrated-circuit packaging, integrated circuits, millimeter wave, passive circuits, transmission-line discontinuities.**

I. INTRODUCTION

Microwave and millimeter-wave circuits and modules (such as front-end receivers) are based on planar technologies using microstrip lines, coplanar waveguides (CPW’s) or finite ground coplanar waveguides (FGCPW’s) since they provide compact, lightweight, and low-loss solutions, and are combined using a wide variety of interconnects such as via holes and air bridges. However, at millimeter-wave frequencies, interconnects, transitions, and packaging techniques become more and more difficult because of the increased influence of discontinuities and substrate losses. Also, unwanted surface waves are more easily triggered into the substrate since the dielectric constant of standard monolithic-microwave integrated-circuit (MMIC) substrates is high ($\epsilon_r = 11.7$ for silicon and 12.9 for GaAs).

This paper presents the experimental and simulation results of two vertical single-layer transitions based on electromagnetic coupling, operating in the W-band region. The first transition was first studied in 1987 by Jackson [1] and uses an overlay of two FGCPW lines to provide an electromagnetic coupling between a CPW mode on the top surface of a substrate to a CPW mode on the bottom surface of the same substrate. The second transition is based on a similar principle and used a short overlay of two coupled-strip lines to provide a surface-to-surface microstrip-mode transition. Both designs are uniplanar and very easy to fabricate since they do not require via holes.

II. W-BAND CPW-TO-CPW TRANSITION

A. Transition Design

The CPW-to-CPW transition described by Jackson [1] consists of an overlay of two FGCPW lines that can support even and odd modes. The dimensions of the overlay region are designed so that the even- and odd-mode impedances result in a perfect match at the frequency of interest. The length of the transition is chosen to be $\lambda_d/4$. Fig. 1(a) shows the perspective view and Fig. 1(b) the cross section of the transition, as well as field distribution for the even and odd modes. The CPW-to-CPW transition has been designed, fabricated, and tested for silicon substrates ($\epsilon_r = 11.7$) in the 75–110-GHz region (Fig. 2). The

---

Manuscript received December 16, 1998. This work was supported by Hughes/Defense Advanced Research Projects Agency under Contract FR-573420-SR8.

The authors are with the Electrical Engineering and Computer Science Department, The University of Michigan at Ann Arbor, Ann Arbor, MI 48109-2122 USA.

Publisher Item Identifier S 0018-9480(00)00230-1.

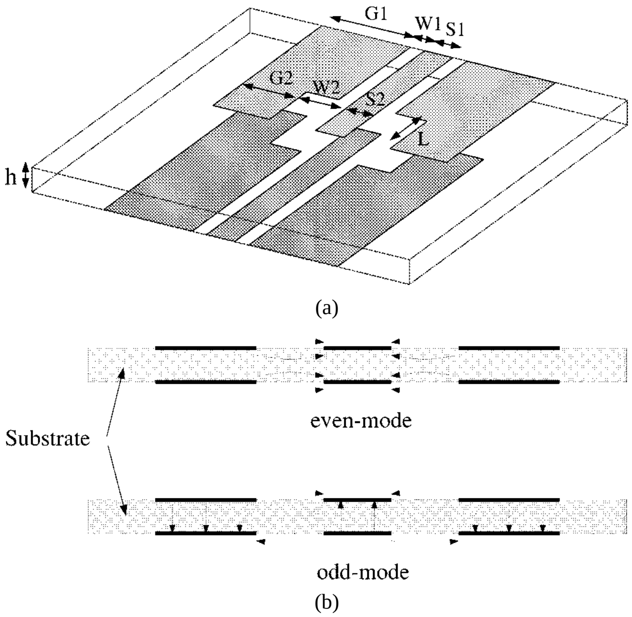

Fig. 1. (a) Perspective view of the CPW-to-CPW single-layer transition. (b) Electric-field configuration for the even and the odd CPW mode.

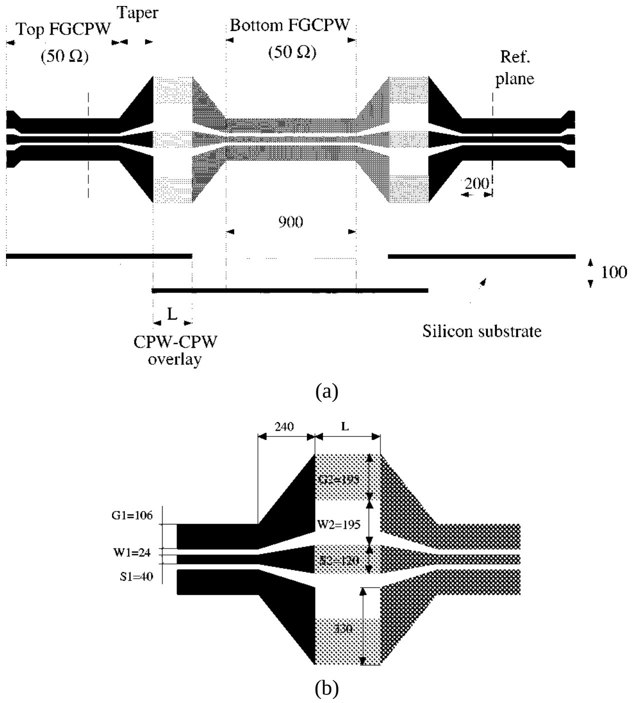

Fig. 2. (a) Layout of the back-to-back CPW-to-CPW transitions. (b) Close view of one single transition. All dimensions are in micrometers.

substrate is 100-μm thick (corresponding to $\lambda_d/9$ at 94 GHz, where λ_d is the dielectric wavelength). The FGCPW input line dimensions are designed to result in a characteristic impedance of 50 Ω. The dimensions of the coupling region are $S2 = 120$ μm, $W2 = 195$ μm, and $G2 = 195$ μm. The coupling region dimensions and the shape of the taper have been numerically optimized with IE3D.[1] To measure the influence of the overlay (coupling) region length on the transition, overlay regions of $L = 210$-, 280-, and 350-µm long are fabricated. The evaporated metal is 8000 Å of gold, corresponding to around three skin depths at 94 GHz.

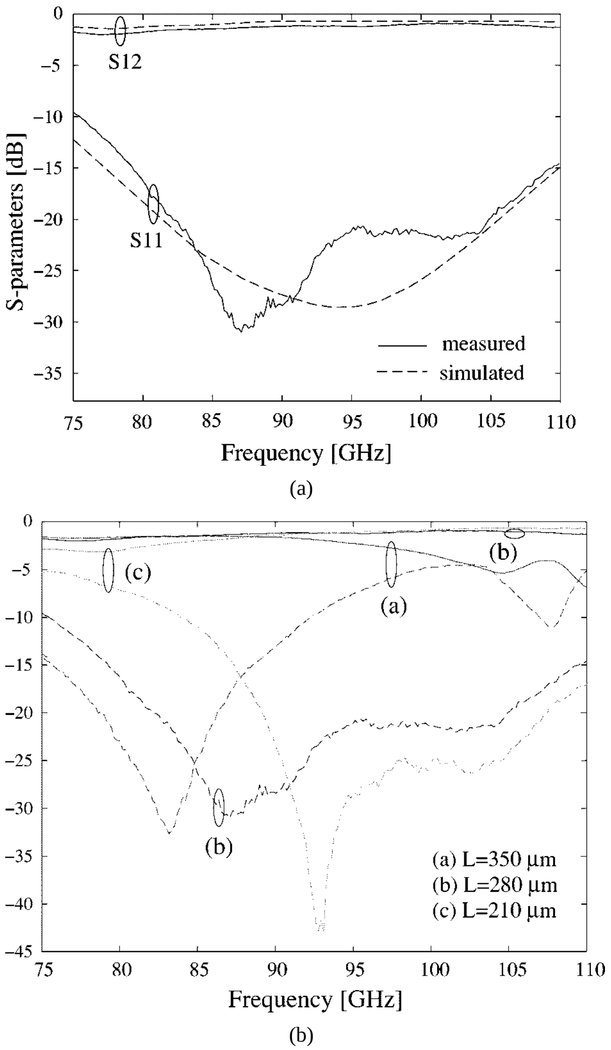

Fig. 3. (a) $\boldsymbol{W}$-band $\boldsymbol{S}$-parameters of back-to-back CPW-to-CPW transitions shown in Fig. 2. (a) Measured and simulated (IE3D) results for an overlay length transition of 280 µm. (b) Measurements for transitions with an overlay length of 210, 280, and 350 µm.

B. *W-Band Measurements*

Vector network analyzer (VNA) measurements of back-to-back transitions separated by a 0.9-mm-long 50-Ω FGCPW line are made using thru-reflection line (TRL) calibration techniques. Fig. 3(a) compares the measurement and simulation (IE3D) results of the CPW-to-CPW vertical transition with an overlay length of 280 µm and Fig. 3(b) presents the measured S-parameters for transitions with three different coupling region lengths. A good agreement is obtained between measurements and simulations (IE3D) from 75 to 110 GHz [see Fig. 3(a)]. Fig. 3(b) clearly shows the bandwidth shift of the transition versus the overlay region length L. The best transition for the 75–110-GHz frequency band is obtained with $L = 280$ μm, which is approximately equal to $\lambda_d/4$ at 96–100 GHz. The total measured loss is –0.9 dB at 100 GHz for $L = 280$ μm, with a return loss below –22 dB. The measured loss for a FGCPW line is 0.35 dB/mm at 94 GHz, thus, the deduced insertion loss per transition is 0.25 dB from 85 to 110 GHz and 0.6 dB over the whole measurement frequency band (75–110 GHz). To our knowledge, this performance is comparable to transitions at 30–60 GHz and presents state-of-the-art values.

---

[1] IE3D Version 4, Zeland Software Inc., Fremont, CA.

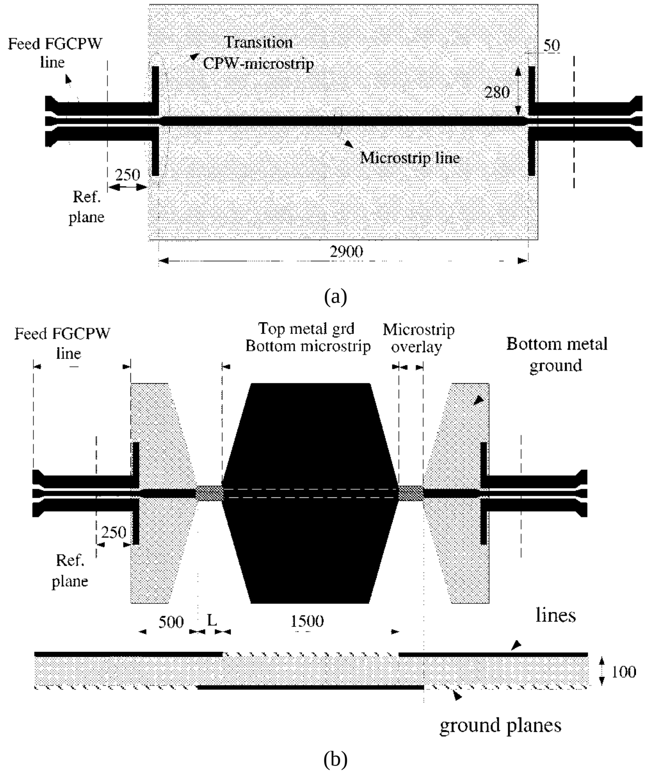

Fig. 4. Layout of back-to-back CPW-to-microstrip transitions including: (a) a microstrip line of 2900-μm long (reference circuit) and (b) back-to-back VMMT's.

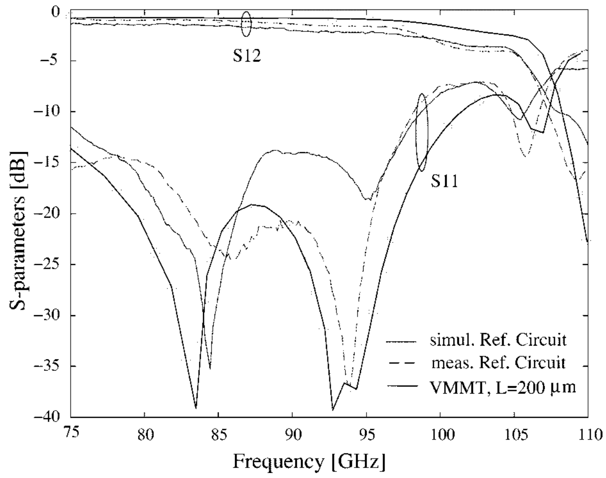

Fig. 5. Measured and simulated (IE3D) back-to-back CPW-to-microstrip transitions including a long microstrip line section (reference circuit). Also included is the measured of back-to-back VMMT's, as shown in Fig. 4(b).

III. W-BAND MICROSTRIP-TO-MICTOSTRIP TRANSITION

A. Transition Design

The second transition presented in this paper uses microstrip-mode coupling. First, a CPW-to-microstrip transition is needed so as to allow W-band coplanar-probe measurements (Fig. 4). The transition is designed following the experimental results presented by Strauss [22]. This type of CPW-to-microstrip transition uses two 90° open stubs (280-μm long) to provide an effective short at the CPW–microstrip interface, and strong field coupling between the FGCPW ground planes and metal backside of the microstrip line. The length of these two stubs is chosen to be $\lambda_d/4$ at the frequency of interest. All dimensions of this transition have been numerically optimized using IE3D for the 75–110-GHz frequency band. The 50-Ω FGCPW input line dimensions are the same as in part II. The microstrip line is 74-μm wide resulting in a characteristic impedance of 50 Ω. The substrate is 100-μm thick. The metal evaporated is 8000 Å of gold.

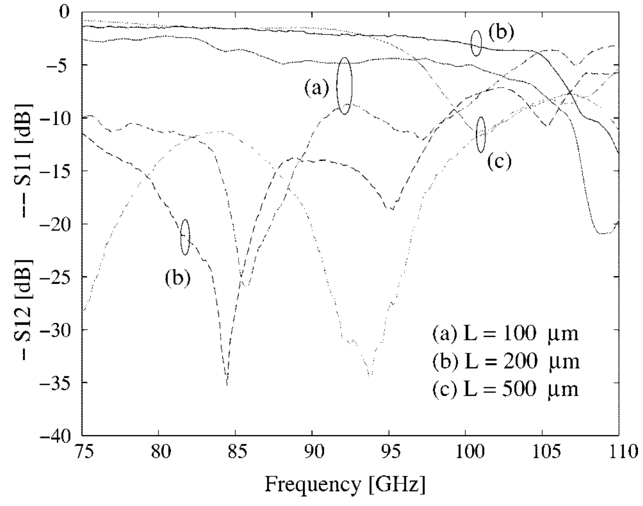

Fig. 6. Measured $\boldsymbol{S}$-parameters of back-to-back VMMT's versus the coupling region length, $\boldsymbol{L}$.

To deembed the insertion loss of the vertical microstrip-to-microstrip transition (VMMT), two circuits having the same total length are fabricated. One is composed of only a simple microstrip section line between the two CPW-to-microstrip transitions [reference circuit, see Fig. 4(a)], and the other includes back-to-back VMMT's [VMMT circuit, see Fig. 4(b)]. With these circuits, the effect of the VMMT can be characterized by a direct comparison. The electromagnetic coupling between the top and bottom microstrip surfaces occurs in the coplanar strip overlay. The coupling region is composed of two coplanar strip lines of 130-μm wide, resulting in a 50-Ω characteristic impedance. To measure the influence of the coupling region length on the microstrip-to-microstrip transition, overlay lengths of 100, 200, and 500 μm have been designed. Preliminary designs were done at 1–2 GHz using a microwave model and then scale to 94 GHz.

B. W-Band Measurements

The microstrip-based transition has been designed, fabricated, and tested for silicon substrates ($\epsilon_r = 11.7$) in the W-band region (75–110 GHz). VNA measurements of two circuits back-to-back transitions are made using TRL calibration techniques (Figs. 5 and 6).

1) CPW-to-Microstrip Transition: Fig. 5 shows a good agreement between the simulations (IE3D) and measurements of the back-to-back CPW-to-microstrip transitions including a long microstrip-line section [Fig. 4(a)]. The measured total loss for the reference circuit is of 0.6 dB at 94 GHz.

2) Microstrip-to-Microstrip Transition: The overlay length of microstrip-to-microstrip transition is $L = 200$ μm. The measured total losses for the circuit with VMMT's [see Fig. 4(b)] and without VMMT's [reference circuit, see Fig. 4(a)] are, respectively, 1 and 0.6 dB at 94 GHz. Therefore, by subtracting the measured losses of these two circuits ($1 - 0.6 = 0.4$ dB), we obtain a loss of 0.2 dB per VMMT at 94 GHz. Fig. 6 presents the measured S-parameters of the back-to-back transition for different overlay lengths. Compared to the overlay length (L) of 200 μm, an increase of around 1.2 dB for the total insertion loss is observed for a reduction of overlay length until 100 μm. The increase of insertion and return losses is attributed to the proximity parasitic coupling between the top and bottom microstrip metal ground plane. On the other hand, a decrease of the transition bandwidth is observed for a longer overlay length ($L = 500$ μm). This is due to the low cutoff frequency of the strip overlay region. Therefore, an optimum overlay length for this VMMT is around 200 µm for W-band applications.

IV. CONCLUSION

Vertical single-layer transitions based on microstrip- or CPW-mode coupling have been developed at W-band frequencies. CPW- and microstrip-mode coupling vertical transitions have shown an insertion loss of better than 0.25 dB (from 85 to 110 GHz) and 0.2 dB (from 75 to 110 GHz), respectively. These transitions can prove very useful for millimeter-wave packaging and vertical interconnects.

REFERENCES

[1] R. W. Jackson and D. W. Matolak, “Surface-to-surface transition via electromagnetic coupling of coplanar waveguides,” *IEEE Trans. Microwave Theory Tech.*, vol. MTT-35, pp. 1027–1032, Nov. 1987.
[2] G. Strauss, P. Ehret, and W. Menzel, “On-wafer measurement of microstrip-based MIMIC’s without via holes,” in *IEEE-MTT-S Int. Microwave Symp. Dig.*, 1996, pp. 1399–1402.